Journal of Solid State Chemistry 255 (2017) 36–41

Contents lists available at ScienceDirect

Journal of Solid State Chemistry

journal homepage: www.elsevier.com/locate/jssc

Structure and color-tunable luminescence properties of Ce^{3+} and Tb^{3+}-activated $Mg_2La_8(SiO_4)_6O_2$ phosphors based on energy transfer behavior

Yuanyuan Zhang[a], Haikun Liu[a], Lefu Mei[a,*], Maxim S. Molokeev[b,c,e], Yongjie Wang[d], Zhaohui Huang[a,*]

[a] Beijing Key Laboratory of Materials Utilization of Nonmetallic Minerals and Solid Wastes, National Laboratory of Mineral Materials, School of Materials Science and Technology, China University of Geosciences, Beijing 100083, China
[b] Laboratory of Crystal Physics, Institute of Physics, SB RAS, Krasnoyarsk 660036, Russia
[c] Department of Physics, Far Eastern State Transport University, Krasnoyarsk 680021, Russia
[d] Institute of Physics, Polish Academy of Sciences, Al. Lotników 32/46, Warsaw 02-668, Poland
[e] Siberian Federal University, Krasnoyarsk 660041, Russia

ARTICLE INFO

Keywords:
Crystal structure
Luminescence properties
Phosphors
Apatite structure

ABSTRACT

A series of novel luminescent emission-tunable phosphors $Mg_2La_8(SiO_4)_6O_2:Ce^{3+},Tb^{3+}$ (MLS:Ce^{3+},Tb^{3+}) have been prepared by a solid-state reaction. The phase formation was firstly confirmed through X-ray diffraction technique and refined by the Rietveld method. The MLS:Ce^{3+},Tb^{3+} phosphors, which crystallized in apatite-type hexagonal phase, exhibited a broad excitation band ranging from 200 to 400 nm and several emission bands centered at 426 nm and 551 nm. Energy transfer from Ce^{3+} to Tb^{3+} ions via a dipole-dipole mechanism occurred in the as-synthesized phosphors upon ultraviolet (UV) excitation. The energy transfer efficiency increases with increasing doping content of Tb^{3+} ions, which was confirmed by the luminescence spectra and fluorescence decay curves of corresponding ions simultaneously. The energy transfer critical distance was calculated and evaluated by both the concentration quenching and spectral overlap methods. The chromaticity of emission-tunable phosphors was also characterized by the Commission International de l'éclairage (CIE) chromaticity indexes, and the color tone can be tuned from blue (0.179, 0.122) to green (0.267, 0.408) by controlling the ratio of Ce^{3+}/Tb^{3+}.

1. Introduction

As an important family of luminescence materials host, the oxy-apatite structure compounds have attracted considerable interest owing to their efficient luminescence as well as excellent chemical and physical stabilities [1–5]. It is well known that oxy-apatite structure compound belongs to the hexagonal symmetrical system (space group of $P6_3/m$) with a general formula as $A_{10}[MO_4]_6O_2$, where A often represents divalent cations such as Ca^{2+}, Ba^{2+}, Sr^{2+}, Mg^{2+}, Pb^{2+}; M represents P, Si, Ge, or V [6–10]. For the $A_{10}[MO_4]_6O_2$ compound, the rare earth ions (RE^{3+}) or alkali metal ions like Na^+, and K^+ can also occupy the A-site because of the isomorphic replacement effect. In terms of a typical member of apatite structure compounds, there are two kinds of cationic crystallographic sites labeled A(1) and A(2) with the local symmetry C_3 and C_s, respectively. A(1) site (Wycoff symbols *4f*) coordinates with nine oxygen atoms to form a tricapped trigonal-prismatic geometry; A(2) site (Wycoff symbols *6h*) coordinates by seven oxygen atoms to build an irregular polyhedron with pentagonal bipyramidal geometry [11–13]. Both A(1) and A(2) sites are certified to be suitable and easily accommodated by a great variety of rare earth and transition metal ions. Additionally, this oxy-apatite structure consists of a free oxygen atom (O4), which locates on the 6-fold axis generally named X site and does not belong to any tetrahedron and only coordinates to three cations in the *6h* sites [14–16]. Therefore, the study on the apatite structure compounds is of significance and valuable, as they possess the capability of being substituted by versatile ions and of forming solid solution. As an important class of apatite structure compounds, $Mg_2La_8(SiO_4)_6O_2$ is isostructural to natural oxyapatite mineral, belongs to the $P6_3/m$ space group with Mg^{2+} and La^{3+} randomly distributed in the *4f* sites and La^{3+} fully occupied the *6h* sites. Hence, in the $Mg_2La_8(SiO_4)_6O_2$ compound, the A(1) and A(2) sites are labeled Mg(1), La(1), and La(2), respectively. The Si atoms were determined to occupy on the *6h* site, and the O atoms were suggested to occupy on the *6h* site (O(1) and O(2)), *12i* site (O3) and *2a* sites (O4). In 1995, Lin' group firstly synthesized the apatite structure compound $Mg_2Y_8(SiO_4)_6O_2$ and revealed the photo-

* Corresponding authors.
E-mail addresses: mlf@cugb.edu.cn (L. Mei), huang118@cugb.edu.cn (Z. Huang).

http://dx.doi.org/10.1016/j.jssc.2017.07.026
Received 18 May 2017; Received in revised form 19 July 2017; Accepted 22 July 2017
Available online 27 July 2017

luminescence of Ce^{3+}, Tb^{3+} and Sm^{3+}, and energy transfer from Ce^{3+} to Tb^{3+}, Dy^{3+} and Sm^{3+} in $Mg_2Y_8(SiO_4)_6O_2$ [17]. They also proved that the $Mg_2Y_8(SiO_4)_6O_2$:Ce^{3+}/Mn^{2+}/Tb^{3+} phosphors show good CL intensity and CIE coordinate stability with a color-tunable emission crossing the whole visible light region under low-voltage electron beam excitation [18]. However, to the best of our knowledge, there are no reports about the detailed photoluminescence properties of rare-earth doped in the MLS host lattice as well as the crystallographic structure information of MLS matrix.

The luminescence properties of Tb^{3+} doped apatite structure compounds have been widely investigated, for instance, $Sr_3Y_2(Si_3O_9)_2$:Tb^{3+} [19], $Ca_5(PO_4)_2SiO_4$:Tb^{3+} [20], $Ba_3NaLa(PO_4)_3F$:Tb^{3+} [21], and $LiRE_9(SiO_4)_6O_2$:Tb^{3+} [22]. In fact, the absorption transition of Tb^{3+} is difficult to pump due to the absolutely forbidden *4–4f* electric dipole transitions [23,24]. As a consequence, Ce^{3+} ions with allowed *5d–4f* transitions are frequently employed to promote the excitation and improve the emission intensity of Tb^{3+} via the energy transfer behavior between Ce^{3+} and Tb^{3+} ions. [25–28]. Herein, we report the detailed photoluminescence (PL) properties of Ce^{3+} and Tb^{3+} in the MLS host lattice as well as the sensitization effect of Ce^{3+}-Tb^{3+} luminescence. Accordingly, the crystallographic data of the MLS compound is firstly reported. The structural properties of the MLS, the luminescence properties and energy transfer mechanism between Ce^{3+} and Tb^{3+} ions have been carried out in details. Furthermore, the emission colors could be tuned from blue to green by changing the concentration of Tb^{3+}.

2. Experimental procedure

$Mg_2La_8(SiO_4)_6O_2$:Ce^{3+},Tb^{3+} phosphors were prepared by a conventional high temperature solid-state method. The raw materials used for the studied phosphors are MgO, SiO_2 (additional H_3BO_3 was added as flux) with analytic grade purity and La_2O_3 (99.99%), Tb_4O_7 (99.99%), CeO_2 (99.99%). Stoichiometric amounts of reactants were thoroughly mixed by grinding in an agate mortar, then the final mixture was placed into an alumina crucible and annealed at 1450 °C in a reducing atmosphere (10% H_2 + 90% N_2) for 3.5 h.

Powder X-ray diffraction (XRD, D8 Advance diffractometer, Bruker Corporation, Germany, 40 kV and 40 mA, Cu Kα λ = 0.15406 nm) was used for phase identification. The step scanning rate (2θ ranging from 5° to 130°) used as structural analysis was 2.5 s per step with a step size of 0.02°. Crystal structure was refined by Rietveld method using the computer software TOPAS 4.2 package [29]. High-resolution transmission electron microscope (HRTEM) images were checked by a JEOL JEM-2010 microscope with an accelerated voltage of 200 kV. The elemental analysis was carried out by energy dispersive spectroscopy (EDS) using an X-ray detector attached to the TEM instrument. Room temperature excitation and emission spectra were measured on a fluorescence spectrophotometer (F-4600, HITACHI, Japan) with a photomultiplier tube operating at 400 V, and a 150 W Xe lamp used as the excitation lamp, a 400 nm cutoff filter was used to eliminate the second-order emission of source radiation in the measurement. The room-temperature luminescence decay curves were obtained from a spectrofluorometer (Horiba, JobinYvon TBXPS) using a tunable pulse laser radiation (nano-LED) as the excitation. All measurements were carried out at room temperature. The relative error in the measurement of fluorescence lifetime is estimated to be ± 2.5%. For data fitting processes also, the error is ± 2.5%.

3. Results and discussion

Fig. 1 shows the observed (solid line), calculated (red circles), and difference (bottom) XRD profiles for the Rietveld refinement of $Mg_2La_8(SiO_4)_6O_2$ at 298 K with λ = 1.5406 Å by TOPAS program. Almost all peaks were indexed by hexagonal cell with parameters close to $Cd_2Nd_8(SiO_4)_6O_2$ (apatite-type structure) [30]. Therefore, the crystal structure of $Cd_2Nd_8(SiO_4)_6O_2$ was taken as the starting model for

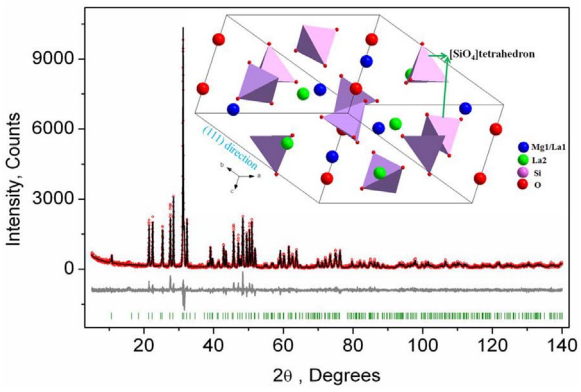

Fig. 1. Rietveld refinement XRD patterns of $Mg_2La_8(SiO_4)_6O_2$ at room temperature by TOPAS program. Solid red circles are calculated intensities, and black lines are the observed intensities. Short vertical lines show the position of Bragg reflections of the calculated pattern. Green solid lines below the profiles stand for the difference between the observed and the calculated intensities. Inset shows crystal structure of $Mg_2La_8(SiO_4)_6O_2$ along the (111) direction. (For interpretation of the references to color in this figure legend, the reader is referred to the web version of this article.)

Table 1
Main parameters of processing and refinement of the $Mg_2La_8(SiO_4)_6O_2$ sample.

Sp.Gr.	$P6_3/m$
a, Å	9.6295(2)
c, Å	7.0687(2)
V, Å^3	567.65(3)
2*θ*-interval, °	5–140
No. of reflections	398
No. of refined parameters	52
R_{wp}, %	18.61
R_p, %	13.88
R_{exp}, %	6.52
χ^2	2.86
R_B, %	7.06

Rietveld refinement. Sites of Cd/Nd ions were occupied by La/Mg ions and the occupations were refined with the assumption that their total in each site equal to 1. Refinement was stable and gives low *R*-factors (Table 1, Fig. 1). Moreover, the refined atomic positions and isotropic temperature factors for all atoms are listed in Table 2. Selected interatomic distances from the refined crystal structure are presented in Table 3. All the experimental peaks were well fitted by the refinement, indicating that all of those peaks are Bragg reflections from the $Mg_2La_8(SiO_4)_6O_2$ structure and converge to R_{exp} = 6.52%, R_{wp} = 18.61%, R_p = 13.88% and χ^2 = 2.86. In the MLS compound, the lattice parameters are determined to be *a* = 9.6295 (2) Å, *c* = 7.0687(2) Å and *V* = 567.65(3) Å^3, respectively. There are two types of cationic sites, one cationic site is labeled as Mg(1)/La(1) which is the *9*-fold coordinated *4f* sites with C_3 point symmetry and the other is labeled as La(2) which is the *7*-fold coordinated 6*h* sites with C_s point symmetry. Hence, the structure of $Mg_2La_8(SiO_4)_6O_2$ can be described as a hexagonal oxyapatite structure with a general composition of

Table 2
Fractional atomic coordinates and isotropic displacement parameters of $Mg_2La_8(SiO_4)_6O_2$.

	x	*y*	*z*	B_{iso}	Occ.
La1	2/3	1/3	0.003 (1)	0.5 (1)	0.48 (2)
Mg1	2/3	1/3	0.003 (1)	0.5 (1)	0.52 (2)
La2	0.2284 (2)	− 0.0144 (3)	1/4	0.8 (1)	1
Si	0.416 (1)	0.374 (1)	1/4	2.2 (3)	1
O1	0.617 (3)	0.460 (3)	0.25	2.1 (4)	1
O2	0.330 (3)	0.513 (3)	0.25	2.1 (4)	1
O3	0.343 (2)	0.267 (2)	0.059 (2)	2.1 (4)	1
O4	0	0	0.25	2.1 (4)	1

Table 3
Selected interatomic bond distances of $Mg_2La_8(SiO_4)_6O_2$ compound.

$Mg_2La_8(SiO_4)_6O_2$	Distances
(La1/Mg1)—O1^{v}	2.32 (2)Å (3×)
(La1/Mg1)—O2^{vi}	2.31 (2)Å (3×)
(La1/Mg1)—O3^{vii}	2.88 (1)Å (3×)
La2—O1^{i}	2.60 (2)Å
La2—O2^{ii}	2.85 (2)Å
La2—O3^{iii}	2.343 (14)Å (2×)
La2—O3^{iv}	2.717 (14)Å (2×)
La2—O4^{ii}	2.272 (2)Å
Si—O1^{iv}	1.68 (2)
Si—O2^{iv}	1.89 (2)
Si—O3^{iv}	1.63 (2)

Symmetry codes: (i) *-y+1, x-y, -z+1/2*; (ii) *-x+y, -x, -z+1/2*; (iii) *y, -x+y, -z*; (iv) *x, y, -z+1/2*; (v) *-x+y+1, -x+1, -z+1/2*; (vi) *-x+1, -y+1, -z*; (vii) *-x+y+1, -x+1, z*.

Table 4
Ionic radii (Å) for given coordination number (CN) of La^{3+}, Ce^{3+}, Tb^{3+}, and Mg^{2+} ions in MLS compound.

Ions	Sites	Symmetry	Ionic radius (Å) CN = 9 (*4f*)	Ionic radius (Å) CN = 7 (*6h*)
La^{3+}	*4f/6h*	C_3/C_S	1.216	1.1
Ce^{3+}	*4f/6h*	C_3/C_S	1.196	1.07
Tb^{3+}	*4f/6h*	C_3/C_S	1.095	0.98
Mg^{2+}	*4f*	C_3	> 0.89	

$[Mg1]_2[La1]_2[La2]_6(SiO_4)_6O_2$. The Mg(1)/La(1) atom is nine-coordinated by nine O atoms with an average Mg1/La1-O distance of 2.50 Å. The La(2) atom is seven-coordinated by seven O atoms with an average La-O distance of 2.549 Å. The Si(1) atoms are tetrahedrally coordinated by four O atoms, which randomly occupy in the *6h* site. The relevant crystal structure along with the (111) direction is shown in the inset of Fig. 1. Based on the effective ionic radii and charge balance of cations with different coordination number (CN) shown in Table 4, the rare-earth Ce^{3+} and Tb^{3+} ions are expected to randomly occupy the La^{3+} ion sites in the MLS host, respectively [31].

The energy dispersive spectroscopy (EDS) was performed to analyze the chemical composition of as-prepared $Mg_2La_8(SiO_4)_6O_2$ phosphor, as shown in Fig. 2, and Mg, La, Si, O, Cu, and C were detected consequently. The results revealed that no extra impurity element was found except for the C and Cu from the electric latex of TEM sample holder, supporting the formation of pure phase of $Mg_2La_8(SiO_4)_6O_2$. The fine local structures of $Mg_2La_8(SiO_4)_6O_2$ were

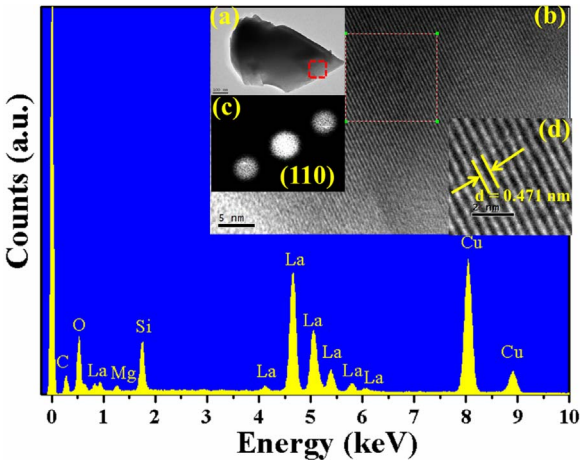

Fig. 2. EDS spectrum of $Mg_2La_8(SiO_4)_6O_2$ powder phosphor. Insert: (a, b) TEM and HRTEM images of $Mg_2La_8(SiO_4)_6O_2$, (c) the fast Fourier transforms (FFTs) of the relevant HRTEM images (d).

also studied by HRTEM technique and the fast Fourier transform (FFT) images are given in Fig. 2a-d. As shown in Fig. 2d, the calculated d spacing of the lattice fringes is 0.471 nm, which could be assigned to the (110), (−120) and (−210) planes with conventional *d* spacing of 0.481 nm in the solved structure of $Mg_2La_8(SiO_4)_6O_2$ compound by Rietveld refinement. As we know, the *d* spacing of (110), (−120) and (−210) planes in apatite structure ($P6_3/m$ space group) represents the same value. Here the (110) plane is chosen to explain the structural evolution between $Mg_2La_8(SiO_4)_6O_2$ and $Cd_2Nd_8(SiO_4)_6O_2$ compound. In this case, the $d_{(110)}$ of $Mg_2La_8(SiO_4)_6O_2$ enlarged ($d_{(110)}$ of 0.478 nm for $Cd_2Nd_8(SiO_4)_6O_2$ compound) slightly owing to the increase of the cell parameters caused by the substitution of Mg^{2+}/La^{3+} for Cd^{2+}/Nd^{3+} ions as compared with the $Cd_2Nd_8(SiO_4)_6O_2$ compound, which is consistent with the result determined by the structural analysis of XRD [30].

Fig. 3a gives the PLE and PL spectra of MLS:0.07Ce^{3+} emphasizing on the two different Ce^{3+} luminescence peaks. Upon 297 nm excitation, the phosphor presents a broad emission band from 400 to 550 nm with the emission peak at 426 nm which can be assigned to the *5d-4f* transition of Ce^{3+} ion. And the PL spectrum of MLS:0.07Ce^{3+} can be well decomposed into four Gaussian components. It is well-known that the Ce^{3+} emission should be consist of a double band in line with the splitting of its ground state, and the theoretical energy difference of this splitting between $^2F_{7/2}$ and $^2F_{5/2}$ of Ce^{3+} is about 2000 cm^{-1} [32–35]. As illustrated in Fig. 3(a), the PL spectrum of MLS:0.07Ce^{3+} excited at 297 nm can be decomposed into four well-decomposed Gaussian components. The former two bands peaked at 405 (24,691 cm^{-1}) and 433 nm (23,094 cm^{-1}) on an energy scale with an energy difference of about 1597 cm^{-1} and the other two bands at 464 (21,552 cm^{-1}) and 519 nm (19,268 cm^{-1}) with an energy difference 2284 cm^{-1}, respectively, which is in agreement with the theoretical difference the splitting between $^2F_{7/2}$ and $^2F_{5/2}$ levels of Ce^{3+}. So the four Gaussian peaks can be ascribed to the *5d-4f* emissions of the Ce^{3+} ions occupied the La(1) and La(2) sites, which is related to its crystal structure, as shown in the insert of Fig. 3a.

As shown in Fig. 3b, upon 226 nm excitation, the emission spectrum illustrates the typical characteristic optical $^5D_4$-^7F_J (J = 6, 5, 4, 3) transitions of Tb^{3+} ions centered at 492, 551, 591, 626 nm. The obvious $^5D_3$-^7F_J (J = 5,6) emissions of Tb^{3+} at 419 and 438 nm are also observed in MLS:0.15Tb^{3+} phosphor, which may results from the lower acoustic phonon energy in this matrix [36,37]. When monitored by the emission of 551 nm, the PLE spectrum of Tb^{3+} consists of several sharp lines in the region from 200 to 525 nm, which is in good agreement with the *4f–4f* absorption transitions of Tb^{3+} ions. On the basis of the comparison of the PLE spectrum of Tb^{3+} and the PL spectrum of Ce^{3+} in Fig. 3c, a spectral overlap can be observed obviously. Therefore, the energy transfer from Ce^{3+} to Tb^{3+} ions is expected in the MLS:Ce^{3+},Tb^{3+} system. In order to confirm the energy transfer phenomenon, the PLE and PL spectra of MLS:Ce^{3+},Tb^{3+} phosphor was recorded, as shown in Fig. 3d. It is observed that the shapes of PLE spectra are similar by using different monitoring wavelength of Ce^{3+} emission and Tb^{3+} emission. The PL spectrum of the MLS:Ce^{3+},Tb^{3+} includes both the emission bands of the Ce^{3+} and Tb^{3+} ions, showing the solid evidence of the occurrence of energy transfer behavior from Ce^{3+} to Tb^{3+}. The schematic diagram of energy transfer (Ce^{3+}→Tb^{3+}) in MLS host upon excitation with UV irradiation is also given in the inset of Fig. 3c. As depicted in this diagram, Ce^{3+} ions can strongly absorb UV light from the ground state ($^2F_{5/2}$) to the excited state and then efficiently transfer the energy to the $^5D_3$ level of Tb^{3+} ions, subsequently, the $^5D_3$ level gives its characteristic transitions or continues to transfer the energy to the $^5D_4$ level via cross relaxation, which is ascribed to the similar value of energy level, and gives the lower vibration frequency of phonon emission [38]. Consequently, a series of color-tunable MLS:Ce^{3+},Tb^{3+} phosphors could be obtained on basis of the energy transfer mechanism between Ce^{3+} and Tb^{3+}.

To investigate the dependence of tunable emission on Tb^{3+}content, a series of MLS:0.07Ce^{3+},yTb^{3+} (y = 0, 0.03, 0.08, 0.15, and 0.25)

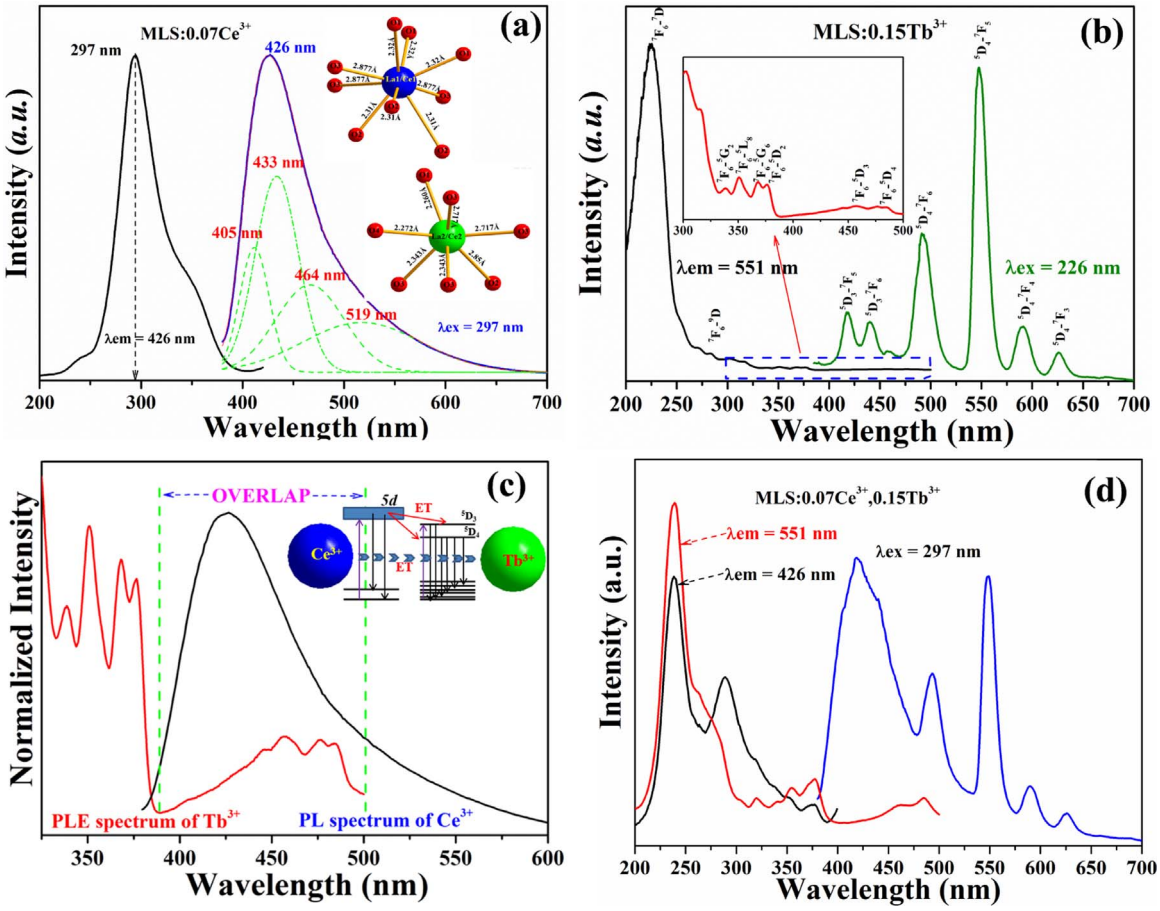

Fig. 3. (a) PL and PLE spectra for MLS:0.07Ce^{3+} emphasizing on the two different Ce^{3+} luminescence centers and their corresponding crystallographic coordination. (b) PL and PLE spectra for MLS:0.15Tb^{3+}. (c) Spectral overlap between the PL spectrum of MLS:0.07Ce^{3+} and the PLE spectrum of MLS:0.15Tb^{3+}, the schematic diagram of energy transfer in MLS:Ce,Tb phosphors is shown in inset of Fig. 3(c). (d) PL and PLE spectra for MLS:0.07Ce^{3+},0.15Tb^{3+} phosphor. The corresponding monitoring wavelengths are also given in the figures.

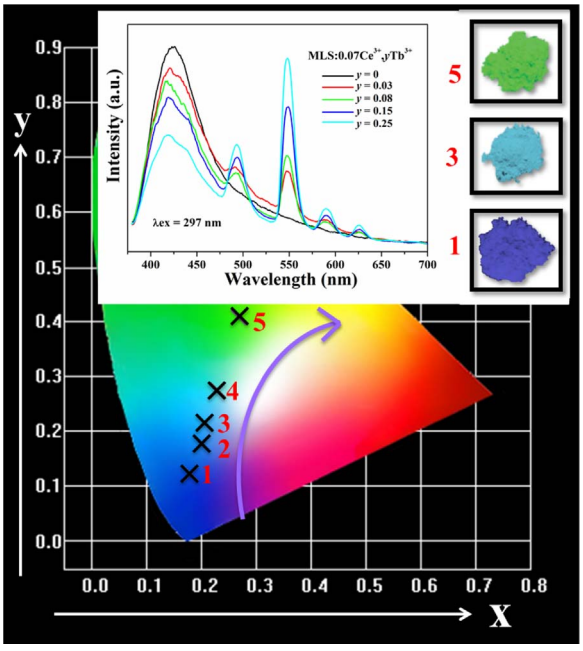

Fig. 4. The CIE chromaticity diagram of the selected MLS:0.07Ce^{3+},yTb^{3+} (y = 0–0.25) phosphors (point 1–5) excited at 297 nm, and a series of digital photographs of color-tunable phosphors are also shown as evidence. (Insert) The PL spectra of MLS:0.07Ce^{3+},yTb^{3+} phosphors as a function of Tb^{3+} doping content (y).

Table 5
CIE chromaticity coordinates (x, y) for MLS:0.07Ce^{3+},yTb^{3+} (y = 0, 0.03, 0.08, 0.15, 0.25) samples (λ_{ex} = 297 nm).

Sample no.	Sample composition (y)	CIE coordinates (x, y)
1	y = 0	(0.179, 0.122)
2	y = 0.03	(0.199, 0.178)
3	y = 0.08	(0.206, 0.214)
4	y = 0.15	(0.230, 0.274)
5	y = 0.25	(0.267, 0.408)

samples have been prepared and the selected dependence of emission spectra for MLS:0.07Ce^{3+},yTb^{3+} excited at 297 nm are depicted in the insert of Fig. 4. It is observed that the luminescence intensity of Ce^{3+} ions decreases monotonically with an increasing of Tb^{3+} concentration, whereas the relative intensity of Tb^{3+} still increases and no concentration quenching occurs, which may attribute to the energy transfer from Ce^{3+} ions to Tb^{3+} ions. Energy transfer makes a feasible route to realize color-tunable emission under excitation of UV light. Therefore, the emission colors could be tuned from blue (0.179, 0.122) to green (0.267, 0.408) in the MLS:0.07Ce^{3+},yTb^{3+} (y = 0, 0.03, 0.08, 0.15, and 0.25) phosphors by varying the ratio of Ce^{3+}/Tb^{3+}. In addition, the corresponding variation of CIE chromaticity coordinates (x, y) with different doping contents of Tb^{3+} on basis of the corresponding PL spectrum and the digital photos of the samples under a 254 nm UV lamp are demonstrated and summarized in Fig. 4 and Table 5. It is clear that the CIE color coordinate of MLS:0.07Ce^{3+},yTb^{3+} phosphors (points 1–5) changes from point 1 (0.179, 0.122) to point 5 (0.267,

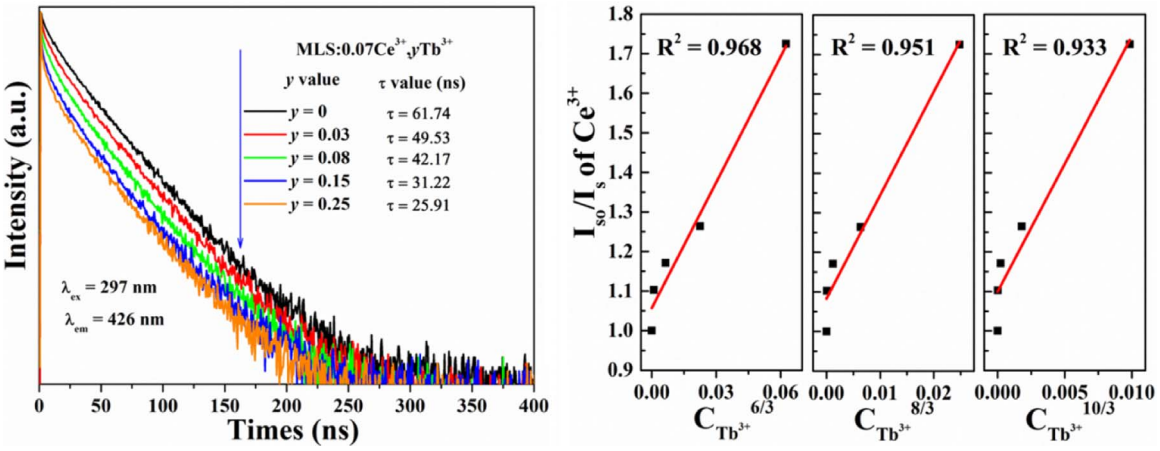

Fig. 5. (a) Decay curves for the luminescence of Ce^{3+} ions in MLS:0.07Ce^{3+},yTb^{3+} samples, the dependence of I_{so}/I_s of Ce^{3+}on (b) $C_{Tb}^{6/3}$ (c) $C_{Tb}^{8/3}$ and (d) $C_{Tb}^{10/3}$. (For interpretation of the references to color in this figure legend, the reader is referred to the web version of this article.)

0.408) with the increasing Tb^{3+} doping contents, which implies the current phosphor has great potential application as a tunable luminescence material to meet the application requirements.

Fig. 5a shows the fluorescence decay curves of Ce^{3+} ions in MLS:0.07Ce^{3+},yTb^{3+} (y = 0, 0.03, 0.08, 0.15, and 0.25) phosphors by monitoring the emission wavelength at 426 nm to validate the energy transfer behavior between Ce^{3+} and Tb^{3+} ions in the MLS lattice. It can be seen that the decay lifetimes of Ce^{3+} ions in the system of MLS:0.07Ce^{3+},yTb^{3+} becomes faster and significantly deviate from exponential decay, which can be fitted successfully with the following typical non-exponential function as below: [39,40]

$$\tau = \frac{\int_0^\infty I(t)tdt}{\int_0^\infty I(t)dt} \quad (1)$$

where $I(t)$ stands for the intensity at time t. Based on the above function, the average decay lifetimes (τ) are determined to be 61.74, 49.53, 42.17, 31.22, and 25.91 ns for MLS:Ce^{3+},Tb^{3+} with different Tb^{3+} concentrations, respectively. Obviously, the decay lifetimes decrease monotonically as the Tb^{3+} concentration increases, which strongly demonstrated the energy transfer from $Ce^{3+}$to Tb^{3+}. Furthermore, the energy transfer efficiency from Ce^{3+} to Tb^{3+} can be calculated based on the following expression: [41–43]

$$\eta_T = 1 - \frac{\tau_x}{\tau_0} \quad (2)$$

where τ_0 and τ_x are the corresponding lifetimes of donor Ce^{3+} in the absence and in the presence of the acceptor Tb^{3+}, and η_T is the energy transfer efficiency. According to the above estimated lifetime and Eq. (2), when the doped Tb^{3+} concentration was fixed at 0.25 mol (y = 0.25), the energy transfer efficiency (η_T) was estimated to be 58.03%. That is to say, the Tb^{3+} emission intensity was enhanced via energy transfer from sensitizer Ce^{3+}, instead of the energy absorption by Tb^{3+} ions themselves. Furthermore, the critical distance of energy transfer R_c was obtained by using the concentration quenching method. As suggested by Blasse, the average separation R_c between $Ce^{3+}$and Tb^{3+}can be estimated according to the following equation: [44]

$$R_c \approx 2\left(\frac{3V}{4\pi x_c N}\right)^{\frac{1}{3}} \quad (3)$$

where N is the number of available sites for the dopant in the unit cell, x_c is defined as the total doping concentration of Ce^{3+} and Tb^{3+} ions at which the emission intensity of the Ce^{3+} ions is half of that of the sample in the absence of Tb^{3+} ions, and V is the volume of the unit cell. In our case of MLS, N equals to 2, and V is estimated to be 567.65 $Å^3$, and the critical doping content x_c, which is defined as the luminescence intensity of Ce^{3+} is half that of the sample in the absence of Tb^{3+} is determined to be 0.32 mol. According to Eq. (3), the critical distance was determined to be around 11.92 Å. The electric multipolar interaction will take place for energy transfer between Ce^{3+} and Tb^{3+} rather than the exchange interaction mechanism in view of the longer distance (more than 5 Å). According to Dexter's energy transfer expressions for the exchange and multipolar interaction, the energy transfer mechanism for multipolar interactions can be evaluated using the following relation:[45]

$$\frac{I_{so}}{I_s} \propto C^{n/3} \quad (4)$$

where I_{so} and I_s are the luminescence intensities of the sensitizer Ce^{3+} with and without activator Tb^{3+}. C is the Tb^{3+}ion dopant concentration. The plots of (I_{so}/I_s) versus $C^{n/3}$ with n = 6, 8, and 10 correspond to dipole-dipole (d-d), dipole-quadrupole (d-q), and quadrupole-quadrupole (q-q) interactions, respectively. The linear (red line) fit to the relationship between I_{so}/I_s and $C^{n/3}$ based on the above equation are illustrated in Fig. 5b. One can see that the R^2 value is closest to 1 when n = 6, which means that the energy transfer from Ce^{3+} to Tb^{3+} follows a nonradiative dipole-dipole interaction. Therefore, according to dipole–dipole interaction mechanism, R_C can be obtained from the following simplified equation: [23,39]

$$Rc^6 = 3.024 \times 10^{12} f_q \int \frac{F_S(E)F_A(E)dE}{E^4} \quad (5)$$

where f_q is the oscillator strength of the involved absorption transition of the acceptor (Tb^{3+}), E is the energy involved in the transfer (in eV), and $\int F_S(E)F_A(E)dE/E^4$ represents the spectral overlap between the normalized shapes of the Ce^{3+} emission $F_S(E)$ and the Tb^{3+} excitation $F_A(E)$. In our case, using the above equation with f_q = 10^{-6}, E was calculated to be about 0.0193 eV^{-4}, and the critical distance R_C was estimated to be 10.95 Å, which agrees approximately with the calculated data that obtained by concentration quenching method (11.92 Å). The result above further confirms that the mechanism of the energy transfer between Ce^{3+} and Tb^{3+} ions is mainly due to a dipole-dipole interaction.

4. Conclusions

In summary, a series of apatite-type structure color-adjustment phosphors MLS:Ce^{3+},Tb^{3+} were prepared by a traditional solid-state reaction. The Rietveld refinement and fine local structure results indicated the as-prepared phosphors crystallized in hexagonal symmetrical system with a space group of $P6_3/m$. The spectroscopic data and fluorescence decay indicated that the energy transfer process could take place from sensitizer Ce^{3+} to activator Tb^{3+} via a nonradiative dipole-

dipole mechanism, and the energy transfer efficiency was also estimated. The critical energy transfer distance has also been calculated by both the concentration quenching method and spectral overlap methods. The emission color of the obtained phosphors can be modulated from blue (0.179, 0.122) to green (0.267, 0.408) by controlling the doping content of the Tb^{3+} ions with the fixed Ce^{3+} content.

Acknowledgment

This present work was supported by the National Natural Science Foundations of China (Grant no. 41172053), the Fundamental Research Funds for the Central Universities (Grant nos. 2652016083 and 2652016037), and Science and Technology Innovation Fund of the China University of Geosciences (Beijing).

References

[1] Y.L. Huang, J.H. Gan, H.J. Seo, J. Am. Ceram. Soc. 94 (2011) 1143.
[2] G. Raju, Y.H. Ko, E. Pavitra, J.S. Yu, J.Y. Park, H.C. Jung, B.K. Moon, Cryst. Growth Des. 16 (2012) 920.
[3] D.L. Geng, H.Z. Lian, M.M. Shang, Y. Zhang, J. Lin, Inorg. Chem. 53 (2014) 2230.
[4] L. Li, Y. Pan, X.J. Zhou, C.L. Zhao, Y.J. Wang, S. Jiang, A. Suchocki, M.G. Brik, J. Alloy. Compd. 685 (2016) 917.
[5] X.G. Zhang, J.L. Zhang, M.L. Gong, Mater. Lett. 143 (2015) 71.
[6] Y.X. Cao, G. Zhu, Y.H. Wang, RSC Adv. 5 (2015) 65710.
[7] F. Zhang, W.J. Tang, Opt. Mater. 37 (2014) 561.
[8] M.M. Shang, D.L. Geng, D.M. Yang, X.J. Kang, Y. Zhang, J. Lin, Inorg. Chem. 52 (2013) 3102.
[9] Q. Su, J. Lin, B. Li, J. Alloy. Compd. 225 (1995) 120.
[10] N. Guo, H.P. You, C.Z. Jia, R.Z. Ouyang, D.H. Wu, Dalton Trans. 43 (2014) 12373.
[11] Y.Q. Shen, R. Chen, F. Xiao, H.D. Sun, A. Tok, Z.L. Dong, J. Solid. State Chem. 183 (2010) 3093.
[12] L. Li, J. Shen, Y. Pan, X.J. Zhou, H. Huang, W.X. Chang, Q.W. He, X.T. Wei, Mater. Res. Bull. 78 (2016) 26.
[13] Y.Q. Shen, R. Chen, G.G. Gurzadyan, J.L. Xu, H.D. Sun, K.A. Khor, Z.L. Dong, Opt. Mater. 34 (2012) 1155.
[14] D. Mazza, M. Tribaudino, A. Delmastro, B. Lebech, J. Solid State Chem. 155 (2000) 389.
[15] G. Zhu, Y.H. Wang, Z.P. Ci, B.T. Liu, Y.R. Shi, S.Y. Xin, J. Electrochem. Soc. 158 (2011) J236.
[16] Y.W. Liu, Z.J. Wang, J.P. Zhong, F.J. Pan, H.B. Liang, Z.G. Xiao, Mater. Lett. 129 (2014) 130.
[17] J. Lin, Q. Su, J. Mater. Chem. 5 (1995) 1151.
[18] Z.Y. Mao, J.J. Chen, L. Sun, Q.F. Lu, D.J. Wang, Mater. Res. Bull. 70 (2015) 908.
[19] M.F. Zhang, Y.J. Liang, S.Y. Xu, Y.L. Zhu, X.Y. Wu, S.Q. Liu, CrysEngComm 18 (2016) 68.
[20] D.L. Geng, M.M. Shang, Y. Zhang, H.Z. Lian, Z.Y. Cheng, J. Lin, J. Mater. Chem. C 1 (2013) 2345.
[21] M.M. Jiao, N. Guo, W. Lv, Y.C. Jia, W.Z. Lv, Q. Zhao, B.Q. Shao, H.P. You, Inorg. Chem. 52 (2013) 10340.
[22] D. Kim, D. Park, N. Oh, J. Kim, E.D. Jeong, S.J. Kim, S.Y. Kim, J.C. Park, Inorg. Chem. 54 (2015) 1325.
[23] I. Couwenberg, K. Binnemans, H. De Leebeeck, C. Gorller-Walrand, J. Alloy. Compd. 274 (1998) 157.
[24] V.V. Atuchin, A.S. Aleksandrovsky, O.D. Chimitova, A.S. Krylov, M.S. Molokeev, B.G. Bazarov, J.,G. Bazarova, Z.G. Xia, Opt. Mater. 36 (2014) 1631.
[25] L.P. Yi, J.L. Zhang, Z.X. Qiu, W.L. Zhou, L.P. Yu, S.X. Lian, RSC Adv. 5 (2015) 67125.
[26] M.J. Xu, L.X. Wang, D.Z. Jia, H.Y. Zhao, Phys. Chem. Chem. Phys. 17 (2015) 28802.
[27] C. Liang, H.P. You, Y.B. Fu, X.M. Teng, K. Liu, J.H. He, Dalton Trans. 44 (2015) 8100.
[28] J. Zhao, C.F. Guo, T. Li, RSC Adv. 5 (2015) 28299.
[29] Bruker AXS TOPAS V4: General profile and structure analysis software for powder diffraction data. – User's Manual. Bruker AXS, Karlsruhe, Germany, 2008.
[30] P.M. Sidorov, E.L. Belokoneva, N.F. Fwedokov, T.A. Tunik, H.A. Simonov, N.V. Belov, Z. Strukt. Khimii. 18 (1977) 397.
[31] R.D. Shannon, Acta Cryst. A 32 (1976) 751.
[32] Z.J. Lu, Z.Y. Mao, J.J. Chen, D.J. Wang, Dalton Trans. 44 (2015) 15620.
[33] W.R. Liu, C.H. Huang, C.P. Wu, Y.C. Chiu, Y.T. Yeh, T.M. Chen, J. Mater. Chem. 21 (2011) 6869.
[34] H. Jing, C.F. Guo, G.G. Zhang, X.Y. Su, Z. Yang, J.H. Jeong, J. Mater. Chem. 22 (2012) 13612.
[35] R.J. Yu, W.J. Ding, G.G. Zhang, J.H. Zhang, J. Wang, J. Alloy. Compd. 509 (2011) 1273.
[36] L.G. Van Uitert, J. Lumin. 29 (1984) 1.
[37] G.G. Li, D.L. Geng, M.M. Shang, Y. Zhang, C. Peng, Z.Y. Cheng, J. Lin, J. Phys. Chem. C 115 (2011) 21882.
[38] Q.H. Zhang, J. Wang, G.G. Zhang, Q. Su, J. Mater. Chem. 19 (2009) 7088.
[39] H.K. Liu, Y. Luo, Z.Y. Mao, L.B. Liao, Z.G. Xia, J. Mater. Chem. C 2 (2014) 1619.
[40] H.K. Liu, Q.F. Guo, L.B. Liao, Z.G. Xia, Opt. Commun. 309 (2013) 64.
[41] F.W. Kang, Y. Zhang, M.Y. Peng, Inorg. Chem. 54 (2015) 1462.
[42] J.H. Zheng, Q.J. Cheng, S.Q. Wu, Z.Q. Guo, Y.X. Zhuang, Y.J. Lu, Y. Li, C. Chen, J. Mater. Chem. C 3 (2015) 11219.
[43] P.C. Chen, F.W. Mo, A.X. Guan, X.H. Liu, L.Y. Tao, J.Q. Tang, J.H. Xu, Y.H. Xu, L.Y. Zhou, Ceram. Inter. 41 (2015) 15005.
[44] N.M. Zhang, C.F. Guo, L.Q. Yin, J.H. Zhang, M.M. Wu, J. Alloy. Compd. 635 (2015) 66.
[45] X.J. Zhang, J. Wang, L. Huang, F.J. Pan, Y. Chen, B.F. Lei, M.Y. Peng, M.M. Wu, ACS Appl. Mater. Interfaces 7 (2015) 10044.